

NMR study of $\text{Ni}_{50+x}\text{Ti}_{50-x}$ strain glassesRui Li ¹, Jacob Santiago,¹ Daniel Salas ², Ibrahim Karaman,² and Joseph H. Ross, Jr. ^{1,2}¹Department of Physics and Astronomy, Texas A&M University, College Station, Texas 77843, USA²Department of Materials Science and Engineering, Texas A&M University, College Station, Texas 77843, USA

(Received 29 December 2022; accepted 10 April 2023; published 28 April 2023)

We studied $\text{Ni}_{50+x}\text{Ti}_{50-x}$ with compositions up to $x = 2$, performing ^{47}Ti and ^{49}Ti nuclear magnetic resonance (NMR) measurements from 4 to 400 K. For large x in this system, a strain glass appears in which frozen ferroelastic nanodomains replace the displacive martensite structural transition. Here, we demonstrate that NMR can provide an extremely effective probe of the strain-glass freezing process, with large changes in NMR line shape due to the effects of random strains which become motionally narrowed at high temperatures. At the same time with high-resolution x-ray diffraction we confirm the lack of structural changes in $x \geq 1.2$ samples, while we show that there is little change in the electronic behavior across the strain-glass freezing temperature. NMR spin-lattice relaxation time (T_1) measurements provide a further measure of the dynamics of the freezing process, and indicate a predominantly thermally activated behavior both above and below the strain-glass freezing temperature. We show that the strain-glass results are consistent with a very small density of critically divergent domains undergoing a Vogel-Fulcher-type freezing process, coexisting with domains exhibiting faster dynamics and stronger pinning.

DOI: [10.1103/PhysRevB.107.144207](https://doi.org/10.1103/PhysRevB.107.144207)**I. INTRODUCTION**

Shape memory alloys (SMAs) have been attractive for decades due to their potential applications in many technological and scientific areas [1]. Among these, NiTi has been one of the most promising materials due to its applications in robotics, biomedical, and aerospace, due to its ability to recover its original shape upon deformation as a result of the reversible martensitic transformation. Stoichiometric NiTi undergoes a first-order phase transition from the high-temperature cubic (CsCl) austenite B2 phase (space group $Pm\bar{3}m$) into the monoclinic martensite B19' phase (space group $P2_1/m$) as temperature decreases (see Fig. 1).

Extensive experimental and theoretical efforts have been made in recent years to tailor martensitic transitions for controlled strain recovery [2–5]. One approach is to turn the abrupt, first-order transformation into a broadly diffused, nearly continuous, strain-glass transition by adding defects. With sufficient surplus Ni content, the martensite transition can be completely suppressed and the $\text{Ni}_{50+x}\text{Ti}_{50-x}$ system becomes a strain glass, characterized by the formation of nanodomains of large local strains (i.e., a strain-glass state) through a freezing transition and exhibits a continuous transformation behavior upon cooling/heating cycling. The strain glass appears to have no martensitic transformation in calorimetry or x-ray diffraction. However, below a well-defined freezing temperature, frequency dispersion of the storage modulus appears in a dynamic mechanical analysis [6–9].

The strain glass is believed to be a kind of ferroic glass, which also includes spin glass and relaxor ferroelectrics [10,11]. Although spin glasses and relaxor ferroelectrics were discovered many decades ago, strain glasses were first identified in 2005 [6] following earlier theoretical work [12,13]

showing that glassy behavior may arise from premartensitic phases above the transformation temperature. These ferroic glasses are defined by disorder of the corresponding order parameters that characterize the associated transformations, i.e., strain in strain glasses, spin in spin glasses, and polarization in relaxor ferroelectrics, thus unlike other structural glasses these glasses emerge from an ordered crystalline state.

Nuclear magnetic resonance (NMR) spectroscopy provides a probe of this behavior on an atomic scale, revealing both static and dynamic information. Here, we have applied this method as a probe of strain-glass dynamics. We performed NMR studies of $\text{Ni}_{50+x}\text{Ti}_{50-x}$ samples from $x = 0.1$ to 2.0, spanning the range from the martensitically transforming to nontransforming strain-glass compositions. In addition, we performed high-resolution x-ray diffraction (XRD) to characterize changes in crystal structure and density functional theory (DFT) calculations to model the electronic structure. As a result we provide information about the thermally activated changes in dynamics that characterize the freezing process.

II. EXPERIMENTAL METHODS**A. Sample preparation**

$\text{Ni}_{50+x}\text{Ti}_{50-x}$ (in at.%) samples include $x = 0.1$ powder fabricated via electrode induction-melting gas atomization (EIGA, from Carpenter Technology Corporation) and $x = 1.2$ bulk material was acquired from Fort Wayne Metals and then gas-atomized by Nanoval GmbH & Company KG. An FEI Quanta 600 FE scanning electron microscope was used to investigate the powder morphology and size distribution. Spherical particles with smooth surfaces and no hollow particles or satellite particles were observed. Mean

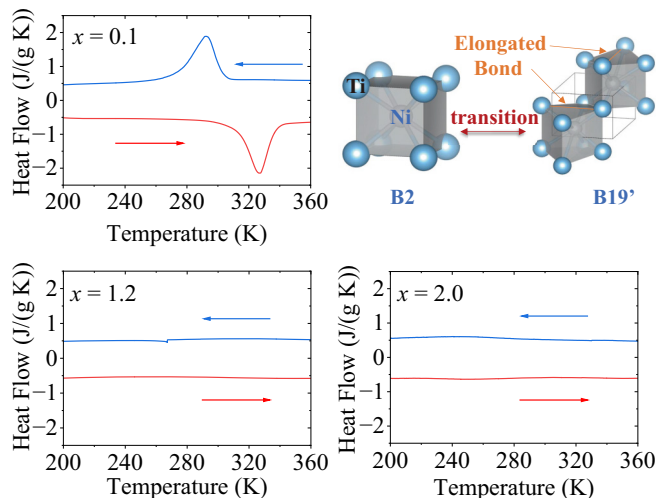


FIG. 1. DSC calorimetry results for three $\text{Ni}_{50+x}\text{Ti}_{50-x}$ samples as shown, with arrows indicating the cooling/heating direction. Latent heat peaks show the well-defined martensitic transition for $x = 0.1$, while no transition is seen for the $x = 1.2$ and 2.0 samples. Upper right: B2 and B19' structures associated with the martensitic transition.

diameters are close to $29\ \mu\text{m}$ for $x = 0.1$ and $20\ \mu\text{m}$ for $x = 1.2$. Both types of powders were wrapped with thin Ta foil and sealed on quartz tubes under a low-pressure high-purity Ar atmosphere. They were homogenized at $1223\ \text{K}$ during 24 h and quenched in room-temperature water. Powders suffered mild sintering and area-limited oxidation. Affected areas were disposed of and the rest was easily repowdered mechanically. For NMR, the powders were sealed in vials with a specimen mass of around 2500 mg. A bulk billet with a nominal $x = 2.0$ content was prepared using vacuum induction melting and then hot rolled at $1173\ \text{K}$ in multiple steps to a 6.35-mm-thick plate. Foils with the dimension of $20\ \text{mm} \times 10\ \text{mm} \times 300\ \mu\text{m}$ were sliced from this plate using wire electrical discharge machining (wire EDM). Following, the foils were sealed on quartz tubes under a low-pressure high-purity Ar atmosphere, heat treated at $1173\ \text{K}$ for 1 h for homogenization, and then quenched in room-temperature water. The NMR testing samples were prepared by stacking ten of these foils and separating them using thin insulating spacers to prevent induced currents.

B. Differential scanning calorimetry (DSC)

Differential scanning calorimetry (DSC) was performed to characterize the transition types using a TA Instruments DSC Q2000 with a cooling/heating rate of $10\ \text{K}/\text{min}$. For $x = 0.1$, the first-order martensitic transformation gives the obvious exothermic and endothermic peaks (Fig. 1) due to the latent heat of transformation. These peaks show thermal hysteresis, as is typical for this material. By contrast, in the $x = 1.2$ and 2.0 samples, the strain-glass transition shows no obvious exothermic and endothermic peaks upon cooling and heating, implying no transformation.

C. X-ray diffraction (XRD)

High-resolution powder x-ray diffraction (XRD) spectra were obtained at the Advanced Photon Source at Argonne Na-

tional Laboratory, with an excitation wavelength $0.459\ 012\ \text{\AA}$. These included $x = 0.1$ and 1.2 samples from the powders processed for NMR, while for $x = 2.0$, one of the foils was wire EDM cut into thin strips which were etched and placed in a Mylar capillary for XRD, with the excitation position translated along the foils during measurement to ensure adequate powder statistics. For $x = 0.1$, measurements at $T = 100$ and $400\ \text{K}$ bracketed the martensitic transformation, while measurements were taken at 100 , 200 , and $295\ \text{K}$ for $x = 1.2$ and 2.0 to sample changes associated with strain-glass freezing. GSAS-II software [14] was used for Rietveld refinement of the resulting patterns.

D. Nuclear magnetic resonance (NMR)

^{47}Ti ($I = 5/2$) and ^{49}Ti ($I = 7/2$) NMR measurements were performed using a custom-built NMR spectrometer at a Larmor frequency $\nu_L(\text{Ti}) = 21.5\ \text{MHz}$ over temperatures from 4 to $400\ \text{K}$. These two NMR isotopes have nearly identical gyromagnetic ratios (γ) so that their spectra overlap. Thus the results shown here are combined NMR spectra, obtained using a standard spin-echo sequence by superposing fast Fourier transformation spectra at a sequence of frequencies. For all displayed spectra, the zero shift position is that of the ^{47}Ti NMR standard (TiCl_4 liquid) calibrated using SrTiO_3 as a secondary NMR reference with its $-843\ \text{ppm}$ NMR shift [15] relative to TiCl_4 .

As is typical for $I > 1/2$ half-integer nuclei, the largest NMR shift is an electric quadrupole shift [16], parametrized by $\nu_Q = \frac{3eQV_{zz}}{2I(2I-1)\hbar}$ and $\eta = (V_{xx} - V_{yy})/V_{zz}$, where V_{jj} are electric field gradients (EFGs) and Q is the nuclear quadrupole moment. In addition, the magnetic shift (K) combines the Knight shift due to susceptibility of the metallic electrons with the chemical shift (conventionally δ) due to susceptibility of filled orbitals. These combine to give a relative shift $K = (\nu - \nu_L)/\nu_L$. The central transition ($1/2 \leftrightarrow -1/2$), displayed for most plotted spectra, is strongest and was used to measure the spin-lattice relaxation time (T_1). In addition, the satellite ($\pm 7/2 \leftrightarrow \pm 5/2$, $\pm 5/2 \leftrightarrow \pm 3/2$, and $\pm 3/2 \leftrightarrow \pm 1/2$) spectra were measured by echo integration.

E. Density functional theory (DFT)

DFT calculations were performed using the linearized augmented plane-wave+local orbitals (LAPW+lo) method as implemented in the WIEN2K code [17,18]. Calculations utilized the Perdew-Burke-Ernzerhof (PBE) functional [19] with a mesh of 1000 irreducible k points, and a cutoff parameter $k_{\text{max}} = 7/\text{RMT}$ inside the interstitial region for plane-wave expansions. These included EFG calculations, a sensitive probe of local strain distortions. Similar calculation methods are typically expected to give close agreement with observed EFGs, for example, within about 10% for comparable intermetallics [20].

III. XRD RESULTS

XRD results are shown in Fig. 2. Small reflections due to Ti_2Ni ($< 1\%$ per mole formula unit) were seen in all samples, which are oxygen-stabilized precipitates typically found in this material [21]. Otherwise refinements show only B2 and

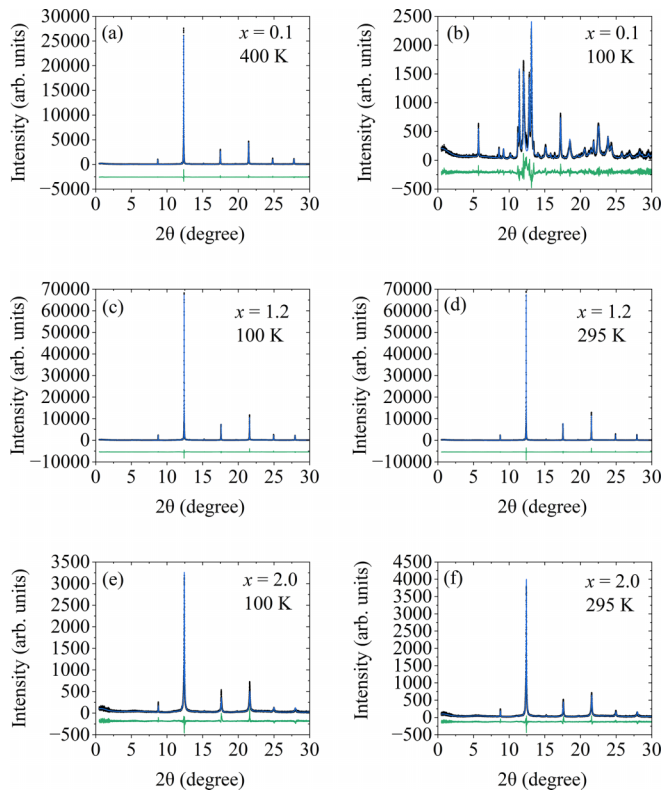


FIG. 2. X-ray powder diffraction data for samples and temperatures indicated. Refined spectra (blue curves) and difference curves (green) also shown. Data residual: $R_w = 8.9\%$, 15.9% , 9.5% , 9.7% , 15.2% , 14.1% for (a)–(f), respectively. Small Ti_2Ni reflections refined to $0.8\%/0.6\%/0.5\%$ per mole formula unit for $x = 0.1/1.2/2.0$, with otherwise only the B19' phase in (b), and the B2 phase in all other refined spectra.

B19' structures [22], with the cubic B2 phase found for the strain-glass compositions at all temperatures, similar to what has been indicated for other strain glasses [23–25].

For $x = 0.1$, the 100 K results fit the expected B19' monoclinic structure [Fig. 2(b)]. The broad feature in the difference curve near 12° may possibly correspond to a small nanostructured R-phase superstructure component (see Supplemental Material [26]), however, there is no evidence for a significant amount of other phases present [38]. Unlike the $x = 0.1$ B2 phase, the peak profiles for the other two samples could not be fitted using the pseudo-Voigt profile of GSAS-II, having instead broader tails flanking each sharp reflection. These were successfully refined in a two-phase model, with sharp reflections combined with those of a second identical B2 phase with large microstrain: For example, the highly strained reflections for $x = 1.2$ refined to a 26% phase fraction, with isotropic microstrain broadening modeled within the GSAS-II package by a $\tan(\theta)$ dependent adjustment of the pseudo-Voigt parameters. The highly strained regions could correspond to the coherent nanodomains [5,39], although this model is intended here mainly as a way to quantify changes in the spectra versus temperature. The fits have almost no temperature dependence. More details, and spectra for other temperatures, are shown in the Supplemental Material [26].

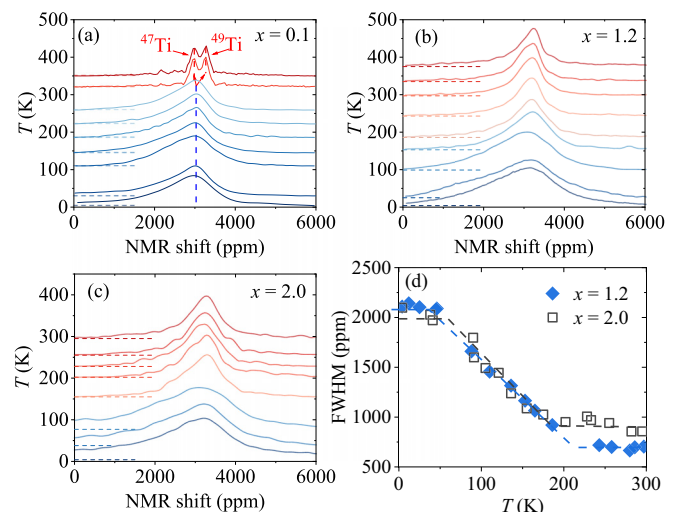


FIG. 3. (a)–(c) ^{47}Ti , ^{49}Ti NMR spectra for $\text{Ni}_{50+x}\text{Ti}_{50-x}$ samples over temperatures from 4 to 400 K, normalized to the same height. For each spectrum, the baseline (dashed line) is positioned at its measurement temperature. (d) Linewidths for strain-glass compositions as measured by the full width at half maximum (FWHM)

IV. NMR RESULTS

A. Line shapes

Figure 3 displays central-transition NMR spectra for the three samples versus temperature. The $x = 0.1$ line shape exhibits a large change near room temperature due to the martensitic transition, above which one can clearly see the separate ^{47}Ti and ^{49}Ti NMR peaks. This is due to the absence of EFGs, and hence narrowing of the quadrupole spectra, in the cubic B2 phase, consistent with previously reported results [40]. For $x = 1.2$ and 2.0 , line broadening sets in [Fig. 3(d)] at temperatures consistent with the onset of strain-glass freezing, despite the absence of changes in XRD. Above this temperature, where electron microscopy results imply an unfrozen strain glass [5], the NMR results are consistent with a broadened B2 phase.

B. NMR shift

NMR shifts versus temperature for the martensitically transforming $x = 0.1$ are shown in Fig. 4. In the martensite phase, the peak intensity positions of the broadened spectra are plotted. The wide-line spectrum measured at 4 K (upper inset) has large tails dominated by electric quadrupole interactions. Least-squares fitting using a custom line-shape program yielded the parameters $\eta = 0.60$, and $^{47}\nu_Q = 775$ kHz/ $^{49}\nu_Q = 300$ kHz (for $^{47}\text{Ti}/^{49}\text{Ti}$, the ratio determined by the corresponding nuclear parameters [41]). These are in close agreement with the previously reported [40] $^{47}\nu_Q = 750$ kHz, $\eta = 0.60$. As a result, we obtained $K = 2820$ ppm at 4 K, slightly larger than the 2700 ppm (renormalized for TiCl_4 standard) previously obtained [40] for the NiTi martensite. For the austenite phase, we obtain $K = 2973$ ppm at 330 K.

For the strain-glass samples, central-transition center of mass (c.m.) shifts are shown in Fig. 5. The c.m. is defined as the intensity-weighted average shift. For these results, the

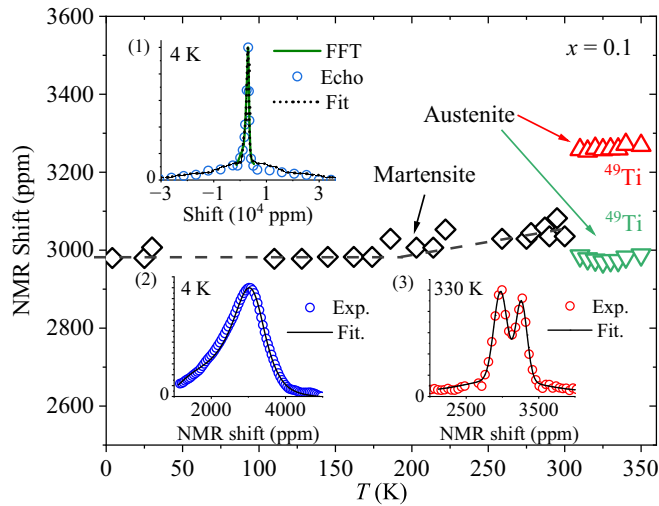


FIG. 4. Warming curve NMR shifts for the $x = 0.1$ sample, relative to the ^{47}Ti standard. Martensite data points are maximum intensity positions of the superposed spectra of the two nuclei. (1) 4-K broad-line spin-echo spectrum with a fast Fourier transformation (FFT) central transition, and the fitted curve described in the text. (2), (3) Fitted 4- and 330-K central-transition FFT spectra.

spectra were fitted using two Gaussian peaks, from which the c.m. shift was calculated. Changes in c.m. correspond to the appearance of enhanced line broadening [Fig. 3(d)] and are due largely to the development of nonzero EFGs at the Ti sites, which induce a negative c.m. shift for the central transition due to second-order electric quadrupole effects [42]. This indicates substantial distortion away from the local cubic environment of the B2 phase. For comparison, the c.m. for the $x = 0.1$ sample is also shown in Fig. 5, clearly indicating the martensite transition near room temperature. The frozen strain-glass spectra can be seen to develop asymmetric line shapes [Figs. 6(a) and 6(b)] accompanying the changes in the c.m. shift.

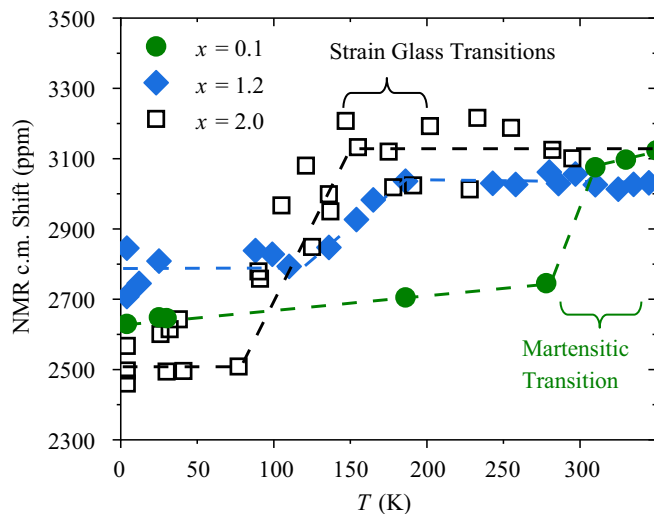


FIG. 5. NMR center of mass (c.m.) shift for the $x = 1.2$ and 2.0 strain-glass samples, as well as c.m. for the $x = 0.1$ martensite transition sample. Dashed lines are guides to the eye.

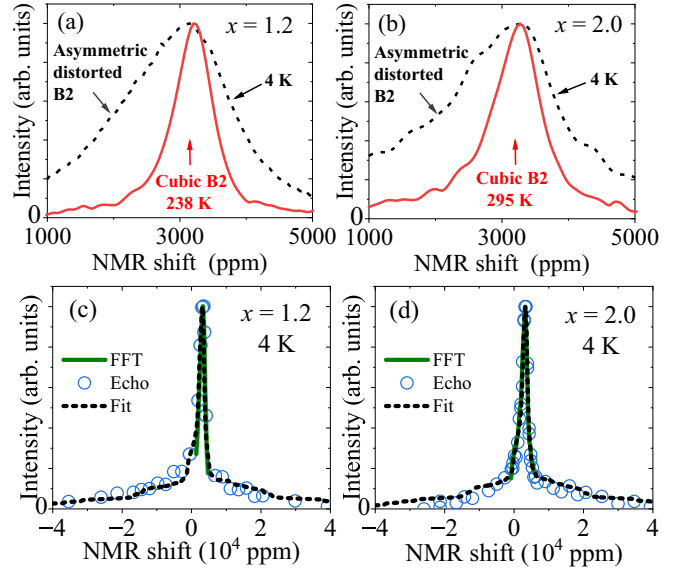


FIG. 6. (a), (b) Ti NMR central-transition spectra for the $x = 1.2$ and 2.0 strain-glass samples, relative to the ^{47}Ti standard. (c), (d) Wide-line spectra, with fits described in the text.

As a quantitative measure of the local-scale asymmetry of the frozen strain glass, we analyzed the low-temperature wide-line spectra [Figs. 6(c) and 6(d)] in a similar manner as described above for $x = 0.1$. Making the simplifying assumption that the strain-glass broadened spectra could be described by a single set of ^{47}Ti NMR parameters, the numerical fits shown yielded $^{47}\nu_Q = 1100$ (1000) kHz and $\eta = 0.70$ (0.75), for $x = 1.2$ (2.0). These larger magnitude EFGs are indicative of atomic-scale asymmetry comparable to that of the coherently distorted B19' phase. The magnetic shifts K are 2950 and 3140 ppm, respectively.

C. Spin-lattice relaxation

The NMR spin-lattice relaxation time (T_1) was measured using a spin-echo inversion-recovery sequence and fitted with a single-exponential curve, $M(t) = (1 - Ae^{-t/T_1})M(\infty)$. Here, $M(t)$ is the measured signal and t is the recovery time. This yielded the $1/T_1$ results shown in Fig. 7. Due to the small signal in the stacked-foil sample, we did not perform similar measurements versus temperature for $x = 2.0$.

For both samples, $(T_1 T)^{-1}$ is constant at low temperatures, a characteristic result for metals referred to as the Korringa process [16,42] due to magnetic interactions with conduction electrons. The increase in relaxation rate at higher temperatures shows the influence of atomic fluctuations, which contribute to $1/T_1$ via electric quadrupole hyperfine interactions. From the temperature dependence and large magnitude of the relaxation rate, particularly in the strain glass, we can rule out phonon-related dynamics [43,44]. For $x = 0.1$, there is a significant further increase in $1/T_1$ at the onset of the phase transition; a narrow $1/T_1$ peak is commonly observed near phase transformations [45] due to critical fluctuations. In relaxor ferroelectrics, in many ways the analogs of strain glasses, a similar peak in $1/T_1$ is often observed near the freezing temperature [46], as will be discussed in more detail

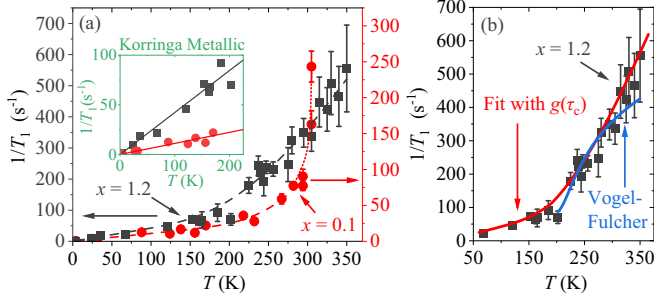


FIG. 7. (a) Fitted single-exponential $1/T_1$ for $x = 0.1$ and 1.2 samples vs temperature. Arrhenius plus Korringa fitted curves are shown by dashed curves. Korringa behaviors are shown by solid lines in the inset. The rapid increase in T_1^{-1} above 300 K for $x = 0.1$ is shown by the dotted line, drawn as a guide to the eye. (b) Vogel-Fulcher and distributed- τ_c fits described in the text.

below. Here, there is no sign of a $1/T_1$ peak at the strain-glass freezing temperature; rather, for both $x = 0.1$ and $x = 1.2$ the results can be interpreted in terms of thermally activated fluctuations, gradually increasing versus T and greatly enhanced in the strain-glass sample.

For a quantitative analysis of the enhanced T_1^{-1} due to fluctuation, we consider a Debye-type relaxation process with a single activated correlation time, equivalent to the Bloembergen, Purcell, and Pound theory [16,47] denoted by $[1/T_1]_{\text{fluct}}$,

$$\left[\frac{1}{T_1} \right]_{\text{fluct}} = 4\pi^2 \nu_{\text{local}}^2 \frac{\tau_c}{1 + \omega_L^2 \tau_c^2}, \quad (1)$$

where $\tau_c^{-1} = f_0 \exp(-\frac{\Delta E}{k_B T})$. Here, ν_{local} is the linewidth, ΔE is the activation energy, f_0 is the attempt frequency, and $\omega_L = 2\pi \nu_L$. Under the assumption that $\nu_L^2 \tau_c^2 \gg 1$, this simplifies to an Arrhenius formula,

$$\left[\frac{1}{T_1} \right]_{\text{fluct}} = f \exp\left(\frac{-\Delta E}{k_B T}\right), \quad (2)$$

where $f = f_0 (\nu_{\text{local}}/\nu_L)^2$. As Fig. 7(a) shows, the experimental data are well fitted over the full temperature range for $x = 1.2$, and below the martensitic transition for $x = 0.1$, by the Arrhenius function plus the Korringa term $[1/T_1]_{\text{K}} = aT$:

$$\frac{1}{T_1} = \left[\frac{1}{T_1} \right]_{\text{fluct}} + \left[\frac{1}{T_1} \right]_{\text{K}} = f \exp\left(\frac{-\Delta E}{k_B T}\right) + aT. \quad (3)$$

The parameters were fitted to be $f = 2.2 \times 10^4$ (5.9×10^3) s⁻¹, $\Delta E = 0.155$ (0.087) eV, and $a = 0.11$ (0.42) (s K)⁻¹ for $x = 0.1$ (1.2). With $\nu_{\text{local}} = 300$ kHz (ν_Q for ⁴⁹Ti which dominates the peak intensity region of the central transition), it is easy to show that $\nu_L \tau_c \gg 1$ over the observed temperature range in both cases, validating the assumption for Arrhenius behavior. The observed attempt frequencies are much smaller than would be expected for single-atom-type hopping, for which f_0 is typically on the order of phonon frequencies, a few THz. Thus the results are consistent with macroscopic domain dynamics rather than that of localized defects or interstitials.

For $x = 0.1$, the results coincide with internal friction measurements [48], interpreted as due to the thermally activated motion of domain walls in the NiTi martensite. The internal

friction results yielded $\Delta E = 0.29 \pm 0.02$ eV for this process, consistent with the result obtained here. There is a limited range for $x = 0.1$ Arrhenius fitting, nevertheless the results behave as expected. It is possible that the factor of $\lesssim 2$ difference is due to a non-Debye behavior for the domain wall relaxation function; a similar result is seen for NMR versus transport results in superionic conductors [49], however, it seems likely that domain wall motion of this type explains the NMR results.

For the $x = 1.2$ strain glass, in the absence of well-defined martensite domains, the thermally activated behavior must instead be due to fluctuating disorder-induced strain. A Vogel-Fulcher-type thermally activated behavior has been reported in strain-glass ac elastic measurements [4,6,8,50], as well as other glass-forming systems [51–55], and is characterized by a modified thermally activated behavior, $\tau_c^{-1} = f_0 e^{-\Delta E/k(T-T_0)}$, where T_0 is typically close to the glass-freezing point. Vogel-Fulcher T dependence has also been used to model the NMR T_1 for freezing processes in polymer glasses and other systems [56–58]. However, generalizing Eq. (3) with the activation term replaced by $f e^{-\Delta E/k(T-T_0)}$, where T_0 was fixed to be 190 K, the fitted curve diverges from the data [Fig. 7(b)], indicating that Vogel-Fulcher behavior is not a good representation for the dynamics as a whole.

V. DISCUSSION

A. Local structure of strain glass

The large low- T linewidths in the strain-glass samples can be understood as due to domains exhibiting strain which fluctuates at high temperatures, thus causing motional narrowing of the NMR spectrum, but which becomes static in the low-temperature limit. Motional narrowing occurs when changes exceed the scale of the NMR linewidth, on the order of 100 kHz (equivalent to ν_{local} defined above). In this way, the apparent discrepancy with XRD results that are essentially T independent can be understood, since the effective response time for XRD measurements is much shorter than that of NMR, so that the magnitudes of the strain within a given domain can appear unchanged in XRD at higher temperatures while in NMR their effect is diminished due to the motional-narrowing averaging process.

The large changes in NMR spectra (Fig. 3) coincide with the reported strain-glass freezing temperatures of about 190 and 170 K for $x = 1.2$ and 2.0 based on a previously reported phase diagram [5,59,60]. On the other hand, the magnetic shift exhibits very little change in the freezing process, e.g., for $x = 2.0$ for which K extracted at 4 K is identical to the high-temperature shift. As K , the local susceptibility, is representative of the electronic behavior, this is an indication that the freezing process does not induce electronic changes, but only slows the dynamics of locally distorted regions.

For further information, we used the WIEN2K package to calculate the EFGs for stable and proposed phases in NiTi. For B19' martensite, similar to a previous report [40], we found that calculated EFGs are larger than what is measured in NMR, with ν_Q ranging from 980 to 1100 kHz for different reported B19' structures [61–63], about 30% larger than the experimental 775 kHz. The strain-glass fitted results described

above are comparable to these calculated B19' values, while for the R phase (space group $P3$) [63], we find somewhat larger calculated EFGs (see Supplemental Material [26]), with a weighted mean $\nu_Q = 1300$ kHz for the Ti sites. These results are both close to the experimental values for the strain-glass materials, so that we cannot obtain a precise indication of the local configuration, however, taking the NMR and XRD results together, it is clear that the distortion of the local structure away from the cubic B2 configuration in the strain glass is significant, with a mean EFG on order of that of the B19' and R structures as compared to B2 with zero EFG.

B. Spin-lattice relaxation and metallic behavior

The low-temperature Korringa T_1 [Fig. 7(a)] indicates a large difference between the metallic behavior of the $x = 0.1$ sample and that of the strain glasses. The larger $1/(T_1T)$ for $x = 1.2$ corresponds to its significantly larger Fermi-level electronic density of states [$g(E_F)$] than B19' martensite. In addition, for $x = 2.0$ we measured $1/(T_1T)$ at a fixed temperature of 4 K. Since the fluctuation spectrum producing the enhanced $1/T_1$ at higher temperatures seems certain to have died out at 4 K as in the other two samples, we assume that the $x = 2.0$ result also represents its metallic behavior.

For a quantitative analysis, the approximate single-exponential recovery curve used above can be replaced by the exact multiexponential central-transition recovery curve for magnetic interactions, which for $I = 7/2$ is given by $M(t) = M(\infty)[1 - A(1.428e^{-\frac{28t}{T_1}} + 0.412e^{-\frac{15t}{T_1}} + 0.136e^{-\frac{6t}{T_1}} + 0.024e^{-\frac{t}{T_1}})]$. The $I = 7/2$ curve is appropriate since ^{49}Ti dominates the NMR signal at the intensity peak, independent of EFG details. Refitted this way, we obtain $1/(T_1T) = 0.0052, 0.017, \text{ and } 0.014$ (s K) $^{-1}$, for $x = 0.1, 1.2, \text{ and } 2.0$, respectively, with $x = 1.2$ and 2.0 strain glasses similarly enhanced relative to the martensite.

A general expression for the Korringa T_1 [64,65] is

$$\left[\frac{1}{T_1T} \right]_{\text{K}} = 4\pi \hbar \gamma_n^2 k_B g_d^2(E_F) \sum_i (H_i^{\text{HF}})^2 F_i, \quad (4)$$

where the sum extends over the hyperfine terms (orbital, core polarization, dipolar) for which H_i^{HF} are the hyperfine fields, γ_n is the nuclear gyromagnetic ratio, $g_d(E_F)$ is the Ti-site local d -electron Fermi level density of states [$g_s(E_F)$ and $g_p(E_F)$ give negligible contributions relative to the d term], and F_i is a numerical factor determined by the mixture of d orbitals [64,65]. For core polarization we use the measured [66] $H_{\text{CP}}^{\text{HF}} = -12.6$ T, while $H_{\text{orb}}^{\text{HF}} = H_{\text{dip}}^{\text{HF}} = +\frac{\mu_0}{4\pi} 2\mu_B \langle r^{-3} \rangle = 25.3$ T, where μ_0 is the permittivity of free space and μ_B is the Bohr magneton, and the calculated $\langle r^{-3} \rangle = 1.36 \times 10^{31} \text{ m}^{-3}$ is used [67]. Note the hyperfine fields differ in sign, giving contributions to the Knight shift which tend to cancel, however, for T_1 , Eq. (4) is a simple sum, with moreover an orbital term which is much larger than the other two, making the analysis unambiguous.

To analyze the results, we calculated $g_d(E_F)$ resolved for individual orbitals, for the B2, B19', and R phases, using the WIEN2K package. General relationships for F_i are given in Ref. [65]; for the case where all five d orbitals are equally weighted at E_F , $F_{\text{orb}} + F_{\text{dip}} = 0.4 + 0.029 = 0.429$ and $F_{\text{CP}} =$

0.2, and we find for all structures the orbital mixtures give results close to these values; full details are given in the Supplemental Material [26]. As a result, we obtained the calculated results $1/(T_1T) = 0.021, 0.0037, \text{ and } 0.015$ (s K) $^{-1}$, for the B2, B19' [62], and R [63] structures, respectively. As the WIEN2K package computes local $g(E_F)$ inside the muffin-tin spheres only, and the additional interstitial contribution is about 20% of the total $g(E_F)$ in these phases, the calculated B19' value is in good agreement with the measured result for $x = 0.1$, with the small observed value confirming the calculated pseudogap in $g(E_F)$ for B19' as previously discussed [38,68,69]. On the other hand, the strain-glass samples have considerably larger Korringa $1/(T_1T)$, and hence larger $g_d(E_F)$ in the frozen state, with the observed $1/(T_1T)$ in good agreement with that of the R phase.

C. Nanodomain fluctuations

Returning to the enhanced $1/T_1$ observed at higher temperatures, the absence of a relaxation peak at the freezing temperature differs from the behavior typically found in relaxor ferroelectrics [46,70,71]. Similarly a peak in $1/T_1$ at the freezing temperature can be observed in some spin-glass systems [72]. In either case, the peak is indicative of a rapid decrease in the characteristic frequency of the fluctuation spectrum, crossing over to a quasistatic spectrum as the temperature crosses the freezing point. The contrasting behavior here indicates a much more gradual slowing down of the fluctuation spectrum over the entire temperature range.

The Arrhenius-type $1/T_1$ analysis described above gives us a probe of these dynamics. Based on the fitted $f = 5.9 \times 10^3 \text{ s}^{-1}$ and $\Delta E = 0.087$ eV for $x = 1.2$ (Sec. IV C), at the freezing point of 190 K we obtain $f \exp(\frac{-\Delta E}{k_B T}) \cong 50 \text{ s}^{-1}$ [Eq. (3)]. Since $f = f_0 (\nu_{\text{local}}/\nu_L)^2$ in Eq. (3), and with $\nu_L = 21$ MHz and $\nu_{\text{local}} \cong ^{49}\nu_Q \cong 300$ kHz (since ^{49}Ti dominates the T_1 relaxation process), we obtain a correlation frequency $\tau_c^{-1} = f_0 \exp(-\Delta E/k_B T) = 200$ kHz at this temperature. As noted above, the criterion for motional narrowing in NMR is that the correlation frequency crosses ν_{local} as it changes versus temperature. For Ti NMR, narrowing will commence when $1/\tau_c$ approached the central-transition width at lower T , and proceed until $1/\tau_c$ exceeds ν_Q . Since τ_c^{-1} obtained here from $1/T_1$ at the freezing point is indeed close to ν_{local} , this shows the consistency between these two results and helps to further validate this model. Thus both the relaxation behavior and the observed NMR line-shape changes point to fluctuating local strain, with a fixed thermal activation barrier, as the process that dominates the local dynamics.

As an alternative model, we examine whether the NMR results can be fitted to a distribution of correlation times rather than a single thermally activated τ_c . This has worked for other systems [73–76] and might account for the Vogel-Fulcher behavior observed in the mechanical relaxation of spin-glass systems [6,77]. Defining $g(\tau_c)$, as the distribution function representing the spatial variation of the fluctuation spectrum, we replace Eq. (1) by the corresponding integration:

$$\left[\frac{1}{T_1} \right]_{\text{fluct}} = \int g(\tau_c) d\tau_c \frac{4\pi^2 \nu_{\text{local}}^2 \tau_c}{1 + \omega_L^2 \tau_c^2}. \quad (5)$$

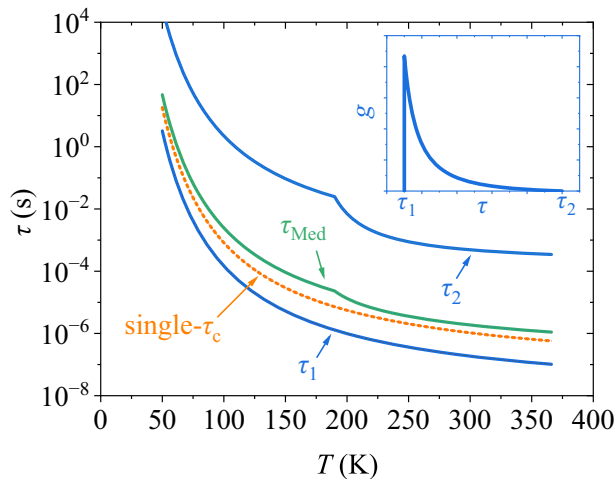


FIG. 8. Limiting parameters for fitted τ_c distribution: τ_1 , τ_2 end points and median value (τ_{Med}). Also, single- τ_c result equivalent to narrow distribution. Inset: Distribution function $g(\tau)$ for the case where $\tau_2/\tau_1 = 10$.

Since the NMR results point to an Arrhenius spectrum, we assume a distribution weighted toward small τ_c for which the temperature dependence is activated, with a large τ_c tail which has a Vogel-Fulcher divergence above the freezing temperature. This is equivalent to a model previously developed for the dielectric behavior of relaxor ferroelectrics [75]. Accordingly, we assigned τ_1 and τ_2 , respectively, as small and large τ_c cutoffs, with the fitted [75] distribution $g(\ln \tau_c) \propto \ln(\tau_2/\tau_c)$ (or equivalently $g(\tau_c) \propto [\ln(\frac{\tau_2}{\tau_c})]/\tau_c$ as plotted in Fig. 8), appropriately normalized.

We set $\tau_1 = \tau_{1,0} e^{1000 \text{ K}/T}$, with activation energy $k_B \times 1000 \text{ K} = 0.087 \text{ eV}$ to match the NMR relaxation results, with the $\tau_{1,0}$ parameter adjusted to fit $1/T_1$, while for τ_2 we use parameters based on internal friction in a NiTi strain glass [6], $\tau_2 = \tau_{2,0} e^{[150 \text{ K}/(T-T_0)]}$, with $T_0 = 160 \text{ K}$ and $\tau_{2,0} = 6 \times 10^{-5} \text{ s}$. Below the glass freezing temperature (190 K for $x = 1.2$), however, the apparent critical divergence of the largest τ_c clusters is interrupted, presumably as they become constrained by neighboring highly pinned regions. To make τ_c continuous versus T we set $\tau_2 = \tau_{2,0} e^{950 \text{ K}/T}$ below 190 K, with the same attempt frequency but modified activation energy due to the arrested divergence.

Fitting the above-described model to the $1/T_1$ results [see Fig. 7(b)] gives $\tau_{1,0} = 7 \times 10^{-9} \text{ s}$. This yields good agreement, similar to the single- τ_c result. The solid curves in Fig. 8 show the corresponding temperature dependence for τ_1 , τ_2 , with the middle solid curve also showing the median value, $\tau_c \equiv \tau_{\text{Med}}$ for this distribution, and the dashed curve showing the fitted dynamics based on the single- τ_c fitting. At 130 K, for example, the latter gives $1/\tau_c = 12 \text{ kHz}$, equivalent to 600 ppm, roughly equal to the central-transition width. At this temperature the linewidth is about halfway between the low-temperature width and the high-temperature narrowed value [Fig. 3(d)] so that as described above these are reasonable values to explain the gradual narrowing process in this temperature regime. At this temperature the distribution

has $1/\tau_{\text{Med}} = 4 \text{ kHz}$ (200 ppm), somewhat smaller than the central-transition width. This suggests that a more complicated distribution function in which the median cluster is unaffected by the divergence would better model this system, however, this distribution captures the general features, considering that the median represents the typical cluster so that the progressive decrease of τ_{Med} vs T implies that a progressively larger fraction of the line becomes narrowed, as observed.

Our results indicate that the Vogel-Fulcher divergence represents a very small fraction of the strain glass in this system, with the majority of the material retaining the relatively fast dynamics required to explain the NMR spectra, extending well below the freezing temperature. This is therefore distinct from the behavior of spin glasses which appear to freeze in a more uniform way [73]. Also, the distribution of dynamical behavior obtained here is more skewed than the distribution which was fitted to the TiPdCr system [76]. We also point out that high-frequency ultrasonic measurements in the TiPdCr strain glass appear to deviate from a Vogel-Fulcher relation [78], as do extended-frequency anelastic studies of $\text{Ni}_{50+x}\text{Ti}_{50-x}$ alloys [79], results which are consistent with the nondivergent behavior of the fluctuation spectrum for small correlation times (e.g., large frequencies) as indicated here. However, our model shows that a low-frequency Vogel-Fulcher-type tail can at the same time be consistent with the storage-modulus results from ac elastic measurements.

VI. CONCLUSIONS

We show that NMR can clearly indicate the freezing process in $\text{Ni}_{50+x}\text{Ti}_{50-x}$, applying this probe to a strain-glass system. The results indicate the development of static local distortions at low temperatures as a slowing-down process, revealing significant local strains in the frozen configuration, with large nuclear electric field gradients comparable to that of the martensite phase despite the absence of a displacive phase transformation. The dynamical unfrozen strain glass causes a large enhancement of the NMR spin-lattice relaxation rate, from which we conclude that the freezing process involves predominantly an Arrhenius process above and below the glass-freezing temperature. Based on a further analysis we present a model for the locally inhomogeneous dynamical strain, which includes a very small density of critically divergent domains involved in the Vogel-Fulcher process, but strongly skewed toward faster dynamics involving more strongly pinned domains.

ACKNOWLEDGMENTS

Support for this project was provided by the Texas A&M University T3 program. Use of the Advanced Photon Source at Argonne National Laboratory was supported by the U.S. Department of Energy, Office of Science, Office of Basic Energy Sciences, under Contract No. DE-AC02-06CH11357. I.K. and D.S. acknowledge the support from U.S. National Science Foundation, under Grant No. DMR-1905325.

- [1] K. Otsuka and C. Wayman, *Shape Memory Materials* (Cambridge University Press, Cambridge, U.K., 1999).
- [2] Y. Ji, P. Zhang, L. He, D. Wang, H. Luo, K. Otsuka, Y. Wang, and X. Ren, *Acta Mater.* **168**, 250 (2019).
- [3] S. Xu, J. Pons, R. Santamarta, I. Karaman, O. Benafan, and R. Noebe, *Acta Mater.* **218**, 117232 (2021).
- [4] D. Wang, Y. Ji, X. Ren, and Y. Wang, *Annu. Rev. Mater. Res.* **52**, 159 (2022).
- [5] Z. Zhang, Y. Wang, D. Wang, Y. Zhou, K. Otsuka, and X. Ren, *Phys. Rev. B* **81**, 224102 (2010).
- [6] S. Sarkar, X. Ren, and K. Otsuka, *Phys. Rev. Lett.* **95**, 205702 (2005).
- [7] J. Cui and X. Ren, *Appl. Phys. Lett.* **105**, 061904 (2014).
- [8] J. Monroe, J. Raymond, X. Xu, M. Nagasako, R. Kainuma, Y. Chumlyakov, R. Arroyave, and I. Karaman, *Acta Mater.* **101**, 107 (2015).
- [9] P. J. Stonaha, I. Karaman, R. Arroyave, D. Salas, N. M. Bruno, Y. Wang, M. F. Chisholm, S. Chi, D. L. Abernathy, Y. I. Chumlyakov, and M. E. Manley, *Phys. Rev. Lett.* **120**, 245701 (2018).
- [10] Y. Ji, D. Wang, Y. Wang, Y. Zhou, D. Xue, K. Otsuka, Y. Wang, and X. Ren, *npj Comput. Mater.* **3**, 43 (2017).
- [11] D. Sherrington, *Phys. Status Solidi B* **251**, 1967 (2014).
- [12] S. Semenovskaya and A. G. Khachatryan, *Phys. Rev. B* **51**, 8409 (1995).
- [13] S. Kartha, T. Castán, J. A. Krumhansl, and J. P. Sethna, *Phys. Rev. Lett.* **67**, 3630 (1991).
- [14] B. H. Toby and R. B. Von Dreele, *J. Appl. Crystallogr.* **46**, 544 (2013).
- [15] C. Gervais, D. Veautier, M. E. Smith, F. Babonneau, P. Belleville, and C. Sanchez, *Solid State Nucl. Magn. Reson.* **26**, 147 (2004).
- [16] C. Slichter, *Principles of Magnetic Resonance, Springer Series in Solid-State Sciences* (Springer Berlin, 1996).
- [17] G. K. H. Madsen, P. Blaha, K. Schwarz, E. Sjöstedt, and L. Nordström, *Phys. Rev. B* **64**, 195134 (2001).
- [18] P. Blaha, K. Schwarz, F. Tran, R. Laskowski, G. K. H. Madsen, and L. D. Marks, *J. Chem. Phys.* **152**, 074101 (2020).
- [19] J. P. Perdew, K. Burke, and M. Ernzerhof, *Phys. Rev. Lett.* **77**, 3865 (1996).
- [20] T. Bastow, M. Burgar, and C. Maunders, *Solid State Commun.* **122**, 629 (2002).
- [21] S. Shabalovskaya, J. Anderegg, and J. Van Humbeeck, *Mater. Sci. Eng., A* **481-482**, 431 (2008).
- [22] K. Otsuka and X. Ren, *Prog. Mater. Sci.* **50**, 511 (2005).
- [23] Y. Wang, X. Ren, and K. Otsuka, *Phys. Rev. Lett.* **97**, 225703 (2006).
- [24] D. Jiang, J. An, Y. Liu, Z. Ma, F. Liu, H. Yang, X. Ren, K. Yu, J. Zhang, X. Jiang, Y. Ren, and L. Cui, *Phys. Rev. B* **104**, 024102 (2021).
- [25] T. Yu, Y. Gao, L. Casalena, P. Anderson, M. Mills, and Y. Wang, *Acta Mater.* **208**, 116651 (2021).
- [26] See Supplemental Material at <http://link.aps.org/supplemental/10.1103/PhysRevB.107.144207> for (1) x-ray diffraction details, including figures showing additional spectra and a more detailed description of the x-ray refinement results, and (2) DFT calculation details, including figures showing calculated partial densities of states, text describing a few additional details about the computation of Korrington T_1 , and a table listing full details of calculated T_1 and electric field gradients, which includes Refs. [27–37].
- [27] Y. Ji, D. Wang, X. Ding, K. Otsuka, and X. Ren, *Phys. Rev. Lett.* **114**, 055701 (2015).
- [28] X. Huang, G. J. Ackland, and K. M. Rabe, *Nat. Mater.* **2**, 307 (2003).
- [29] J. Mentz, J. Frenzel, M. F.-X. Wagner, K. Neuking, G. Eggeler, H. P. Buchkremer, and D. Stöver, *Mater. Sci. Eng., A* **491**, 270 (2008).
- [30] Z. Deng, Q. Li, Y. Onuki, and Q. Sun, *J. Alloys Compd.* **909**, 164682 (2022).
- [31] K. Fukami-Ushiro and D. Dunand, *Metall. Mater. Trans. A* **27**, 193 (1996).
- [32] P. Bogdanoff and B. Fultz, *Philos. Mag. B* **81**, 299 (2001).
- [33] S. Qiu, V. Krishnan, S. Padula, R. Noebe, D. Brown, B. Clausen, and R. Vaidyanathan, *Appl. Phys. Lett.* **95**, 141906 (2009).
- [34] N. Ashcroft, N. Mermin, and N. Mermin, *Solid State Physics* (Holt, Rinehart and Winston, New York, 1976).
- [35] B. Fultz, *Prog. Mater. Sci.* **55**, 247 (2010).
- [36] F. Yu and Y. Liu, *Computation* **7**, 57 (2019).
- [37] N. Singh, A. Talapatra, A. Junkaew, T. Duong, S. Gibbons, S. Li, H. Thawabi, E. Olivos, and R. Arróyave, *Comput. Mater. Sci.* **112**, 347 (2016).
- [38] A. Kunzmann, J. Frenzel, U. Wolff, J. Han, L. Giebeler, D. Piorunek, M. Mittendorff, J. Scheiter, H. Reith, N. Perez, K. Nielsch, G. Eggeler, and G. Schierning, *Mater. Today Phys.* **24**, 100671 (2022).
- [39] N. de Mathan, E. Husson, G. Calvarn, J. R. Gavari, A. W. Hewat, and A. Morell, *J. Phys.: Condens. Matter* **3**, 8159 (1991).
- [40] T. Bastow and G. West, *J. Phys.: Condens. Matter* **15**, 8389 (2003).
- [41] R. K. Harris, E. D. Becker, S. M. C. de Menezes, R. Goodfellow, and P. Granger, *Pure Appl. Chem.* **73**, 1795 (2001).
- [42] G. C. Carter, L. H. Bennett, and D. J. Kahan, *Metallic Shifts in NMR* (Pergamon, Oxford, U.K., 1977).
- [43] A. Hackmann and O. Kanert, *Radiat. Eff. Defects Solids* **119-121**, 651 (1991).
- [44] X. Zheng, S. Y. Rodriguez, and J. H. Ross, *Phys. Rev. B* **84**, 024303 (2011).
- [45] A. Rigamonti, *Adv. Phys.* **33**, 115 (1984).
- [46] R. Blinc, A. Gregorovič, B. Zalar, R. Pirc, V. V. Laguta, and M. D. Glinchuk, *Phys. Rev. B* **63**, 024104 (2000).
- [47] N. Bloembergen, E. M. Purcell, and R. V. Pound, *Phys. Rev.* **73**, 679 (1948).
- [48] B. Coluzzi, A. Biscarini, G. Mazzolai, and F. Mazzolai, *Mater. Sci. Eng., A* **442**, 414 (2006).
- [49] J. Boyce and B. Huberman, *Phys. Rep.* **51**, 189 (1979).
- [50] J. Liu and X. Jin, *Phys. Status Solidi B* **251**, 2055 (2014).
- [51] R. Pirc and R. Blinc, *Phys. Rev. B* **76**, 020101(R) (2007).
- [52] J. W. Schmelzer and T. V. Tropin, *Entropy* **20**, 103 (2018).
- [53] W. Xu, J. F. Douglas, and Z. Sun, *Macromolecules* **54**, 3001 (2021).
- [54] S. A. Morley, D. Alba Venero, J. M. Porro, S. T. Riley, A. Stein, P. Steadman, R. L. Stamps, S. Langridge, and C. H. Marrows, *Phys. Rev. B* **95**, 104422 (2017).
- [55] A. Pramanick and S. Nayak, *J. Mater. Res.* **36**, 1015 (2021).
- [56] R. Nefati, P. Judeinstein, and J. Rault, *J. Phys.: Condens. Matter* **32**, 465101 (2020).

- [57] M. E. Ries, P. G. Klein, M. G. Brereton, and I. M. Ward, *Macromolecules* **31**, 4950 (1998).
- [58] S. Wu, X. Liang, Y. Lei, L. Yang, L. Wang, and J. Feng, *J. Phys. Chem. Lett.* **11**, 6039 (2020).
- [59] P. Bag, P.-C. Chang, Y.-K. Kuo, S.-K. Wu, C. Lin, and B.-Y. Li, *Intermetallics* **109**, 16 (2019).
- [60] X. Ren, Y. Wang, Y. Zhou, Z. Zhang, D. Wang, G. Fan, K. Otsuka, T. Suzuki, Y. Ji, J. Zhang, Y. Tian, S. Hou, and X. Ding, *Philos. Mag.* **90**, 141 (2010).
- [61] W. Buhner, R. Gotthardt, A. Kulik, O. Mercier, and F. Staub, *J. Phys. F: Met. Phys.* **13**, L77 (1983).
- [62] Y. Kudoh, M. Tokonami, S. Miyazaki, and K. Otsuka, *Acta Metall.* **33**, 2049 (1985).
- [63] H. Sitepu, *Powder Diffr.* **24**, 315 (2009).
- [64] Y. Obata, *J. Phys. Soc. Jpn.* **18**, 1020 (1963).
- [65] B. Nowak, *Solid State Nucl. Magn. Reson.* **21**, 53 (2002).
- [66] B. Nowak, O. Zogal, and K. Niedzwiedz, *J. Alloys Compd.* **186**, 53 (1992).
- [67] A. Koh and D. Miller, *At. Data Nucl. Data Tables* **33**, 235 (1985).
- [68] Y. Y. Ye, C. T. Chan, and K. M. Ho, *Phys. Rev. B* **56**, 3678 (1997).
- [69] T. Fukuda, *Mater. Trans.* **61**, 33 (2020).
- [70] F. Cordero, M. Corti, F. Craciun, C. Galassi, D. Piazza, and F. Tabak, *Phys. Rev. B* **71**, 094112 (2005).
- [71] R. Blinc, A. Gregorovič, B. Zalar, R. Pirc, and S. G. Lushnikov, *Phys. Rev. B* **61**, 253 (2000).
- [72] S. Kundu, T. Dey, A. V. Mahajan, and N. Büttgen, *J. Phys.: Condens. Matter* **32**, 115601 (2019).
- [73] K. Binder and A. P. Young, *Rev. Mod. Phys.* **58**, 801 (1986).
- [74] Z. G. Lu and G. Calvarin, *Phys. Rev. B* **51**, 2694 (1995).
- [75] A. Levstik, Z. Kutnjak, C. Filipič, and R. Pirc, *Phys. Rev. B* **57**, 11204 (1998).
- [76] Y. Zhou, Y. Wang, D. Xue, X. Ding, J. Sun, X. Ren, and T. Lookman, *J. Phys.: Condens. Matter* **30**, 345402 (2018).
- [77] Y. Ji, X. Ding, T. Lookman, K. Otsuka, and X. Ren, *Phys. Rev. B* **87**, 104110 (2013).
- [78] S. L. Driver, E. K. H. Salje, C. J. Howard, G. I. Lampronti, X. Ding, and M. A. Carpenter, *Phys. Rev. B* **102**, 014105 (2020).
- [79] S. Kustov, D. Salas, E. Cesari, R. Santamarta, D. Mari, and J. Van Humbeeck, *Acta Mater.* **73**, 275 (2014).